Effectiveness of a lattice discrete element model to simulate mechanical wave shielding by using barriers into the ground

Sabrina Vantadori[a,*], Andrea Carpinteri[a], Ignacio Iturrioz[b]

[a] Department of Civil and Environmental Engineering & Architecture, University of Parma, Parco Area delle Scienze 181/A, 43124 Parma, Italy
[b] Mechanical Post-Graduate Program, Federal University of Rio Grande do Sul(UFRGS), Sarmento Leite 425, Porto Alegre, Brazil

ABSTRACT

Several vibration sources can provoke propagation of mechanical waves into the ground. Such waves have to be taken into account both in designing of new buildings and in shielding of strategic structures. The vibration control systems may be either active systems or passive systems such as vertical barriers. One of the main problems encountered in the numerical simulation of wave shielding by using vertical barriers is the ground modeling. To such an aim, the method originally formulated by Riera is here employed to simulate both typical elastic-dynamic problems and a complex problem consisting in the numerical simulation of a vertical barrier wave shielding into a damaged ground where wave propagation occurs.

1. Introduction

Several vibration sources as traffic, machine foundations, explosions, and earthquakes can provoke propagation of mechanical waves in the ground [1,2]. Such waves should be taken into account both in designing of new buildings and in shielding of strategic structures. The vibration control systems able to improve the structure behavior regarding failure induced by vibrations may be either active systems, which impose forces on the structure that counterbalance the vibration induced forces by requiring an energy source, or passive systems, which do not require any additional energy source to operate and are activated by the vibration input.

The wave barriers, named barriers in the following, are passive systems able to absorb a significant portion of the dynamic energy arising from the ground motion. Such barriers are structural components placed into the ground, and may be of different types: vertical barriers (including open trenches) and rough surfaces [3,4], horizontal barriers [5,6], and rows of piles [7].

The problem of wave shielding was extensively examined from both a numerical and an experimental point of view in the context of the train-induced ground vibrations [8–11]. More precisely, Çelebi et al. [12] performed experimental tests by examining the basic characteristics of the wave propagation, and proposed some suitable countermeasures able to reduce ground soil vibrations. Tsai et al. [13] analyzed both open trenches and diaphragm-wall barriers by applying the 2D Boundary Element Method. Alzawi et al. [14] performed full scale experimental tests to analyze vibration scattering by employing both open trenches and GeoFoam barriers. Xia et al. [15] analytically examined how cylindrical piles could influence elastic waves scattering. Ekanayake et al. [16] numerically investigated the efficiency level of different barrier materials to mitigate ground vibrations, and Saikia [17] studied vibration screening effectiveness using in-filled trenches.

One of the main problems encountered in the numerical simulation of wave shielding by using barriers is the ground modeling. The numerical methods proposed in the literature to simulate a continuous medium can be classified in two main groups: (i) methods

Nomenclature

		respectively	
A_d	cross-section of diagonal bars	L_d	length of diagonal bars
A_n	cross-section of longitudinal bars	L_n	length of longitudinal bars
A_{i*}	equivalent fracture area for the diagonal $(i = d)$	$\mathbf{M}$	mass matrix
	and longitudinal $(i = n)$ bars	$\mathbf{P}(t)$	vector of internal nodal forces
$\mathbf{C}$	damping matrix	$\dot{\mathbf{x}}(t)$	velocity vector
CV_{G_f}	coefficient of variation of G_f	$\ddot{\mathbf{x}}(t)$	acceleration vector
d_{eq}	characteristic length of the material	v_P, v_S, v_R	dilatational, shear, and Rayleigh wave velocity,
E	elastic modulus of the ground		respectively.
E_b	elastic modulus of the barrier	ε	bar strain
f_{max}	maximum frequency	ε_r	ultimate tensile strain
f_p	frequency at peak energy dissipation spectrum	ε_p	bar strain at the peak load
$f(G_f)$	probability distribution of G_f	ξ	damping ratio
F_b	bar axial force	λ_{min}	minimum wave length
$\mathbf{F}(t)$	vector of external nodal forces	ν	Poisson coefficient of the ground
G_f	specific fracture energy	ν_b	Poisson coefficient of the vertical barrier
$H[\cdot]$	Heaviside function	ρ	ground density
k	wave number $(k = 1/\lambda)$	ρ_b	barrier density
L_{cx}, L_{cy}, L_{cz}	correlation length of G_f in x, y, z direction,		

based on the Continuum Mechanics, and (ii) the so-called Discrete Element Methods.

The group of methods based on the Continuum Mechanics includes the Finite Element Method and the Boundary Element Method, where both elastic and elastic-plastic behavior can carefully be modelled and damage can also be included into the model by using an extension of the constitutive equations employed in plasticity [18]. Such methods have been extensively applied to simulate wave propagation problems as, for example, in the work by Liu et al [19]. However, it is also possible to simulate the material properties as random fields, as is shown in Ref. [20], but some limitations to describe the damage evolution in quasi-fragile materials are encountered. As a matter of fact, in the damage process of quasi-fragile materials (such as rocks and some types of ground) the transition from continuous to discontinuous material has to be taken into account, but methods based on a hypothesis of continuous medium have difficulty to follow such a transition. On the other hand, the assumption of the ground as a homogeneous and isotropic medium could be too simplified.

The group of the so-called Discrete Element Methods includes methods that do not need to assume a continuous medium. As a matter of fact, both the heterogeneity and the anisotropy of the medium can be implemented by means of scalar fields to be used for the material properties [21]. Note that the medium heterogeneity may also be implemented by applying a pre-stress condition to the medium, generating heterogeneity patterns [22]. There are many discrete element methods available in the literature, and a review of them is given in Ref. [23]. According to such methods, the medium is simulated by discretising it through an array of nodes, where the masses are concentrated at nodes, masses generally interacting through nonlinear potentials within the realm of the Newtonian dynamics. The philosophy behind such methods is the same on which the particle methods are founded. In the last two decades, the Peridinamics approach has been used in the context of the Discrete Element Methods to solve typical engineering problems. This approach, originally presented by Silling [24], can be employed to evaluate fracture, fragmentation and damage, in both quasi-elastic and transient problems. Several applications of such an approach are also reported in Refs [25,26]. Even in the field of rock mechanics, the above approach is used to simulate the damage evolution in rocks and soils [27,28].

Another option to link the aforementioned nodes is by means of an array of bars. Methods related to such an approach are named Lattice Discrete Element Methods [29–33].

In the present paper, the method originally formulated by Riera [34] (Lattice Discrete Element Method, named only LDEM in the following) is employed to simulate the wave shielding produced by a vertical barrier into a damaged ground where wave propagation
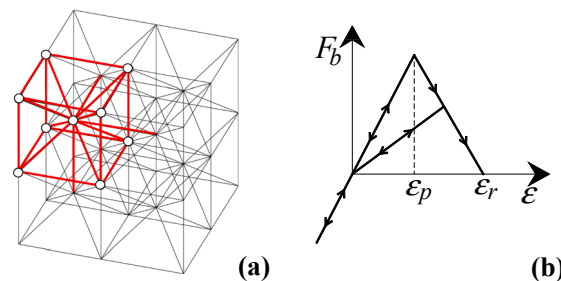

Fig. 1. LDEM model: (a) cubic arrangement of nodes and massless uniaxial elements, (b) bilinear constitutive relationship for both diagonal and longitudinal bars.

occurs. Several papers available in the literature employ such a method to simulate an impact test performed on a Polymethyl Methacrylate disk [35], an impulsive loading acting on both plain and reinforced concrete structures [36–40], acoustic emission tests [41–44], and earthquakes [45–48], but no paper on the wave shielding produced by a vertical barrier has been published.

The present paper is organized as follows. Firstly, the basic concepts of the LDEM are presented (Section 2). Then, the capability of the LDEM to solve typical elastic-dynamic problems is discussed (Section 3). Finally, the LDEM is applied to a complex problem aimed to show the effectiveness of the LDEM to simulate the wave shielding of a vertical barrier into a damaged ground where wave propagation occurs (Section 4). Conclusions are summarized in Section 5.

2. The lattice discrete element method (LDEM): Basic concepts

The LDEM allows us to model a continuous medium (named medium in the following) as an 3D-array of nodes linked by massless uniaxial elements (or bars) able to carry only axial load. These bars are organized in a cubic arrangement (Fig. 1a) that is, cubic cells with nine nodes [34]. Such an arrangement was firstly proposed by Nayfeh et al. in 1978 [49] to determine the properties of an orthotropic elastic medium, as is specified in the following.

The discretized masses assumed concentrated at nodes have three degrees of freedom, represented by the displacements in three orthogonal directions. According to the above arrangement, the length of longitudinal and diagonal bars are L_n and $L_d = L_n \sqrt{3}/2$, respectively.

The stiffness of each bar is linked to the properties of the isotropic elastic medium by the following equations [35,49]:

$$\frac{EA_n}{L_n} = E\phi L_n \tag{1}$$

$$\frac{EA_d}{L_d} = \frac{4\delta}{3} E\phi L_n \tag{2}$$

where

$$\phi = \frac{9 + 8\delta}{18 + 24\delta} \tag{3}$$

$$\delta = \frac{9\nu}{(4 - 8\nu)} \tag{4}$$

being E and ν the elastic modulus and the Poisson coefficient of the material, respectively, and A_d and A_n the cross-section of each diagonal and longitudinal bar, respectively.

The discretized equation of motion according to the Newton's second law is given by:

$$\mathbf{M}\ddot{\mathbf{x}}(t) + \mathbf{C}\dot{\mathbf{x}}(t) + \mathbf{F}(t) - \mathbf{P}(t) = 0 \tag{5}$$

where the vectors $\ddot{\mathbf{x}}(t)$ and $\dot{\mathbf{x}}(t)$ represent the nodal acceleration and velocity, respectively, $\mathbf{M}$ and $\mathbf{C}$ are the mass and damping matrices, respectively, and the vectors $\mathbf{F}(t)$ and $\mathbf{P}(t)$ are the internal and external nodal forces, respectively. The damping matrix $\mathbf{C}$ is given by:

$$\mathbf{C} = 2\pi \, \xi \, f_p \, \mathbf{M} \tag{6}$$

where ξ is the damping ratio, and f_p is the frequency at peak value of the energy spectrum.

Since $\mathbf{M}$ and $\mathbf{C}$ are diagonal matrices, the scalar equations corresponding to the vector given by Eq. (5) are integrated in the time domain by using an explicit finite difference scheme. Note that, since nodal coordinates are updated at each time step t, they can directly be computed from the above equations without any additional computation even in the case of large displacements, since rotations are not degrees of freedom of the model.

The LDEM is particularly suitable to simulate the presence of cracks, which can be implemented into the model as either pre-existing flaws or in terms of bar damage.

In the last case above, a non-linear constitutive law for bars has to be defined. The damage consists in breaking of the bars when they attain a critical condition according to the softening law for quasi-brittle material proposed by Hillerborg [50]. Such a law, assumed for both longitudinal and diagonal bars, is the bilinear constitutive relationship shown in Fig. 1(b), where F_b is the bar axial force and ε is the axial strain.

The bar critical condition is reached when ε is equal to or greater than ε_r (Fig. 1(b)), equal to:

$$\varepsilon_r = \varepsilon_p d_{eq} \left(\frac{A_i^*}{A_i}\right)\left(\frac{2}{L_i}\right) \tag{7}$$

where ε_p is the strain at the peak load, d_{eq} is a characteristic material length, i identifies the type of bar ($i = d$ for diagonal bar, and $i = n$ for longitudinal bar), L_i is the bar length, A_i is the bar cross-section, and A_i^* is the equivalent fracture area of the i-th bar.

The equivalent fracture area A_n^* is deduced by equating the dissipated energy U_d^c in a cubic continuum specimen (of sizes $L_n \times L_n \times L_n$) because of a fracture along a plane parallel to one of its faces

$$U_d^c = G_f \cdot L_n^2 \tag{8}$$

to the dissipated energy in a LDEM cell (of sizes $L_n \times L_n \times L_n$) along the same fracture plane:

$$U_d^{LDEM} = G_f \left[4 \cdot \left(\frac{1}{4} \right) \cdot A_n^* + A_n^* + 4 \cdot A_n^* \cdot \left(\frac{2}{\sqrt{3}} \right)^2 \right] L_n^2 \tag{9}$$

being G_f the specific fracture energy. More precisely, the first term into the square brackets accounts for the contribution of the four external longitudinal bars of the LDEM cell (each of them sheared with other four adjacent cells, as is shown Fig. 1(a)); the second term accounts for the internal longitudinal bar (the vertical one in Fig. 1(a)); the third term accounts for the four diagonal bars, where the factor $(2/\sqrt{3})^2$ is included in order to take into account that (i) the diagonal bars are fractured along sections forming an angle different from zero with respect to the corresponding cross-sections, and (ii) the diagonal bar fracture Modes occur. Details are given in Ref. [43].

Therefore, by equating Eq. (8) with Eq. (9):

$$A_n^* = \frac{3}{22} L_n^2 \tag{10}$$

and consequently:

$$A_d^* = \left(\frac{2}{\sqrt{3}} \right)^2 A_n^* = \frac{4}{22} L_n^2 \tag{11}$$

Therefore, the bar is considered as broken when the bar strain ε is equal to or greater than ε_r. Note that the bar behavior under compression is assumed to be linear elastic and, although the failure under compression is not allowed, a tensile failure can occur due to the transversal tension stresses produced by the axial compression.

The strain at the peak load, ε_p, is computed as follows:

$$\varepsilon_p = \sqrt{\frac{\mu_{G_f}}{E \, d_{eq}}} \tag{12}$$

where μ_{G_f} is the mean value of the specific fracture energy G_f.

When the length of at least one of the cracks developing in the modeled body exceeds the material critical length d_{eq} [43], unstable crack propagation occurs. Note that the presence of a crack is simulated by adjacent broken bars in the model. More details
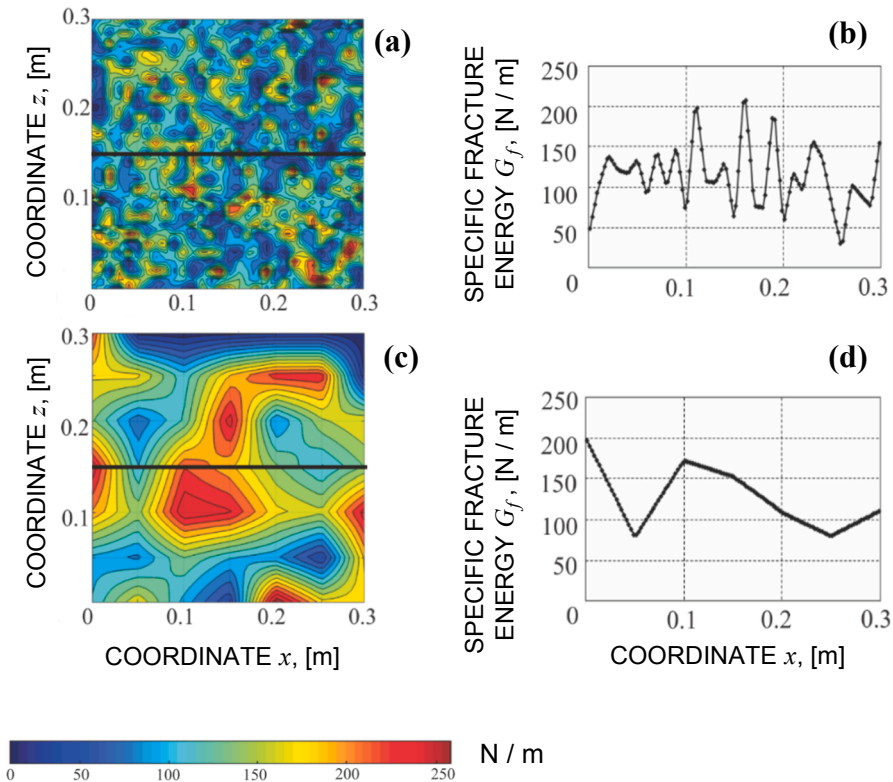

Fig. 2. Distribution of G_f: (a) bi-dimensional and (b) mono-dimensional (for $z = 0$) distribution by using $L_{cx} = L_{cz} = 2L_n$ with $L_n = 0.005\,\text{m}$; (c) bi-dimensional and (d) mono-dimensional (for $z = 0$) distribution by using $L_{cx} = L_{cz} = 10L_n$ with $L_n = 0.005\,\text{m}$.

can also be found in Refs [21,35].

In the LDEM, G_f is assumed to have a Weibull probability distribution given by:

$$p(G_f) = 1 - exp[-(G_f/\beta)^\gamma] \tag{13}$$

being β and γ the scale and shape parameters, respectively. Such parameters can be computed through the coefficient of variation CV_{G_f}, defined as the ratio between the standard deviation s_{G_f} and the mean value μ_{G_f} of the specific fracture energy G_f.

However, a spatial correlation function for G_f needs to be defined. The correlation lengths L_{cx}, L_{cy} and L_{cz} along the three directions x, y, z, respectively, are used to such an aim. Details may be found in Refs [21,43].

As an example, let us consider the case study reported in Ref. [21], consisting in a square body with a side of 0.3 m, analyzed in plane strain condition. Fig. 2 shows the bi-dimensional distribution of G_f employed in the such a work, for two pairs of values of the correlation lengths L_{cx} and L_{cz}.

3. Basic simulations by using the LDEM

In the present Section, the propagation of dilatational, shear, and Rayleigh waves into the ground are analyzed by using the LDEM, in order to state that the LDEM is able to quite carefully model typical problems related to ground vibration.

3.1. Simulation No.1

3.1.1. Ground model through the LDEM

Now the ground, assumed as an isotropic and homogeneous medium, is modelled as a prism (see Fig. 3) with length of 120 m (in x-direction), width of 24 m (in z-direction), and depth of 2.5 m (in y-direction).

The mechanical properties of the ground are assumed to be as follows: $E = 0.33$ GPa, $\nu = 0.25$ and density $\rho = 1750$ kg/m^3, corresponding to a ground composed by a dense sand.

Symmetry boundary conditions are applied to the yz plane corresponding to $x = 0$, and to the xz plane corresponding to $y = \pm1.25$ m (see Fig. 3). Note that, in the case of non-homogeneous medium, such boundary conditions allow us to carefully model the actual ground avoiding to reduce the problem to a plane strain problem, for $-1.25 \leqslant y \leqslant 1.25$ m. In order to avoid the wave reflection phenomenon, total absorption boundary condition is applied to both the xy plane (corresponding to $z = 0$) and the yz plane (corresponding to $x = 120$ m).

The frequency range of waves here analyzed is equal to [0,50] Hz.

By using the basic equations of elastodynamics [51], the velocities of dilatational, shear and Raleigh waves are respectively given by:

$$v_P = \sqrt{\frac{E(1-\nu)}{\rho(1+\nu)(1-2\nu)}} \tag{14}$$

$$v_S = \sqrt{\frac{E}{2\rho(1+\nu)}} \tag{15}$$

$$v_R = \frac{0.87 + 1.12\nu}{(1+\nu)} v_S \tag{16}$$

For the problem being examined, such velocities are equal to $v_P = 475.70$ m/s, $v_S = 274.64$ m/s, and $v_R = 252.67$ m/s.
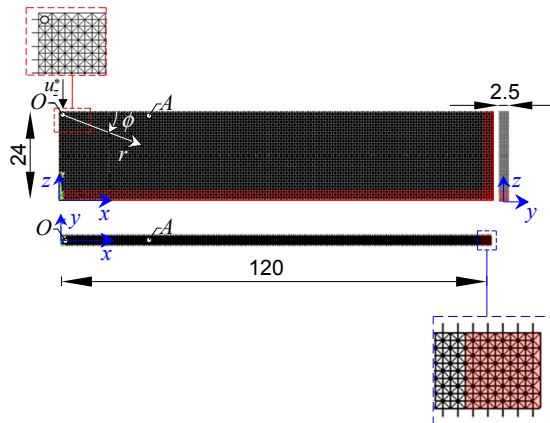

Fig. 3. LDEM model used in the basic simulation No.1: sizes are in m. The region of total absorption boundary condition is highlighted in red. Details of the discretisation employed are also shown.

Then, the minimum wave length λ_{min} is computed as follows:

$$\lambda_{min} = v_R/f_{max} = 5.05 \text{ m} \qquad (17)$$

being $f_{max} = 50$ Hz.

According to Aberg et al. [52], the bar length L_n has to be chosen in a range defined by $1/10\ \lambda_{min}$ and $1/8\ \lambda_{min}$. Then, L_n is assumed to be equal to 0.50 m, and $240 \times 48 \times 5$ cubic cells are employed in x, y and z-direction, respectively, to generate the LDEM model shown in Fig. 3.

The excitation is assumed to be acting at point O with coordinates equal to (0.25; 0.0; 23.75) m (Fig. 3), and the model response is captured at point A with coordinates equal to (24.75; 0.0; 23.75) m. The excitation is applied to the model through a displacement in z-direction, given by [53]:

$$u_z^* = u_0\ sin(2\pi ft)\ sin\left[\frac{\pi(t - t_a)}{t_d}\right]H(t - t_a)\ H(t_b - t) \qquad (18)$$

where u_0 is the amplitude of the signal, t_a and t_b represent the time instants when the excitation starts and stops, respectively, $t_d = t_b - t_a$ is the corresponding time interval, and $H[\cdot]$ represents the Heaviside function. A graphical representation of such an excitation is shown in Fig. 4 for $u_0 = 2$ mm, $t_a = 0.02$ s, $t_b = 0.12$ s, and $f = 50$ Hz. In such a figure, the displacement u_z^* is normalised with respect to its maximum value ($u_{z,max}^* = 1.98$ mm).

Note that, for time instants greater than t_b, point O is left free to vibrate.

3.1.2. Results

For the numerical model described in Section 3.1.1, the results obtained in terms of displacements are shown in Fig. 5. More precisely, the model response at point A in terms of both horizontal u_x and vertical displacement u_z is plotted in Fig. 5(a). The theoretical time instants at which each wave type reaches point A are highlighted with grey vertical lines in Fig. 5, where the label t_P refers to the dilatational wave, t_S to the shear wave, and t_R to the Rayleigh wave.

It can be observed in Fig. 5(a) that the dilatational wave arrives at point A at time instant equal to $t_P = 0.051$ s, in accordance with the theoretical value. The sudden increase in u_z displacement, due to the Rayleigh wave arrival, is attained at time instant $t_R = 0.097s$ in accordance with the theoretical evaluation, whereas it is not possible to identify the time instant of the shear wave arrival by using such a model. Therefore, only to solve last problem, an additional restriction is added to the numerical model described in Section 3.1.1, that is, the displacement in x-direction is fixed for all nodes. In such a way, only the shear wave propagates and, as is shown in Fig. 5(b), the time instant of its arrival at point A agrees with the theoretical value ($t_S = 0.089$ s).

Now the model response in terms of displacement at the nodes located at an average radial distance equal to 24 m from point O is analyzed. A polar frame (ϕ, r) is used to identify such nodes (see Fig. 3). The mean value of the magnitude of the dilatational wave velocity along the path characterized by $r \cong 24$ m and $0° \leqslant \phi \leqslant 45°$ is computed: $\mu_{v_P} = 519.72$ m/s. Then the numerical magnitudes v_P related those nodes along the above path are divided by μ_{v_P} and, by plotting such a ratio against the angular coordinate ϕ, it can be observed in Fig. 6 that the influence of the mesh orientation (by varying the ϕ angle value) on the wave velocity is negligible, being the v_P value lower than or greater than μ_{v_P} by no more than about 2%.

In Fig. 7, the Fast Fourier Transform (FFT) of the vertical displacement u_z is plotted in the dispersion curve domain represented by the frequency f against the wave number $k = 1/\lambda$. In order to draw such a graph, the vertical displacement is registered during a time interval from 0 to 0.5 s (time step equal to $7(10)^{-5}$ s) in 200 points lying on a horizontal segment delimited by points having coordinates equal to (10.75; 0.0; 23.75)m and to (110.75; 0.0; 23.75)m. More precisely, firstly such data are used to build a matrix in time-space domain, each row containing the vertical displacement related to the above 200 points at a given time instant (matrix size equal to 7142×200). Then, by applying the FFT to such a matrix, a new matrix is obtained in frequency-space domain. Finally, by applying again the FFT to the last matrix, a matrix in the frequency-wave number domain is determined. Details about the procedure
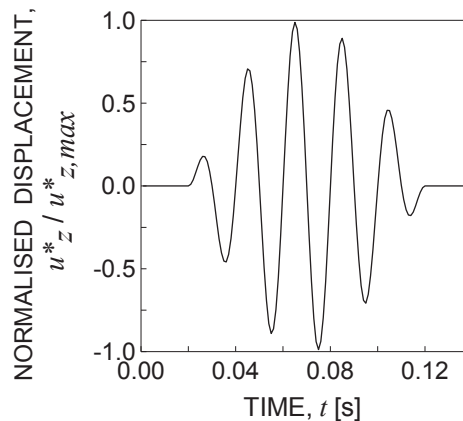

Fig. 4. Plot of the function given in Eq.(15), for $u_0 = 2$ mm, $t_a = 0.02$ s, $t_b = 0.12$ s, and $f = 50Hz$.
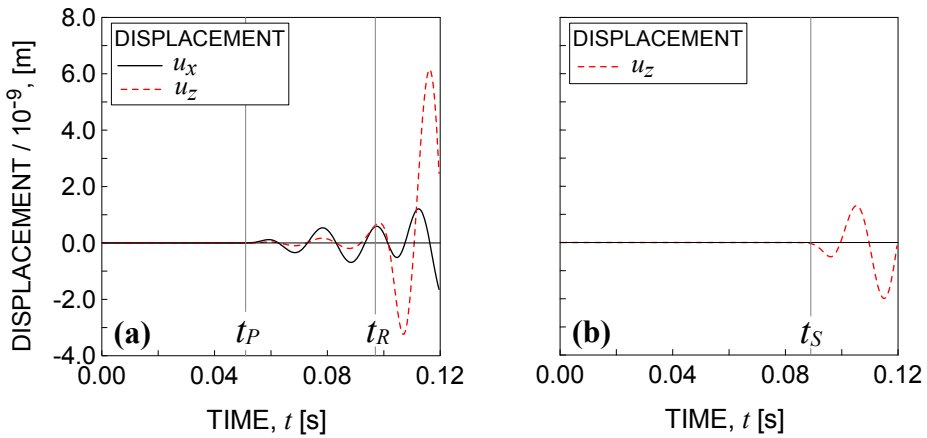
Fig. 5. Numerical response at point A in terms of: (a) horizontal and vertical displacements, and (b) vertical displacement produced by the shear wave.
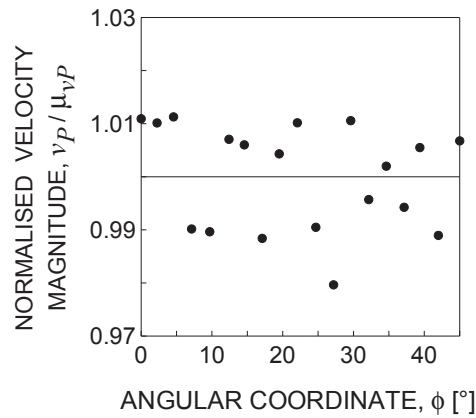

Fig. 6. Plot of the normalised velocity magnitude v_P/μ_{vP} of the dilatational wave vs the coordinate ϕ.
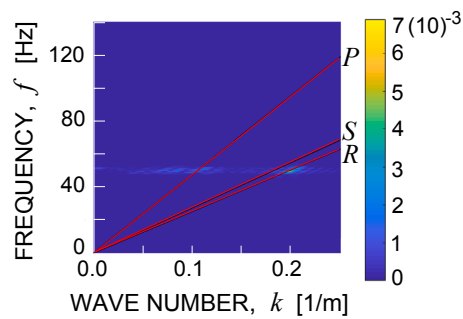

Fig. 7. Fast Fourier Transform (FFT) of vertical displacement u_z (expressed in m) plotted in the dispersion curve domain, represented by frequency vs wave number.

adopted my be found in Ref. [54].

Further, the theoretical dispersion curves related to the dilatational, shear and Rayleigh waves are plotted (see three red lines in Fig. 7). It can be observed that the maximum value of u_z is attained at frequency of 50 Hz and at wave length of about 5 m ($k = 0.2/$m) for the Rayleigh wave, and at wave length of 10 m ($k = 0.1/$m) for the dilation wave.

3.2. Simulation No. 2

3.2.1. Ground model through the LDEM

The ground is modelled as is described in Section 3.1.1. With respect to Simulation No.1, a vertical barrier is included into the

ground. The vertical barrier has depth of 5 m and width of 0.5 m. The barrier is assumed to be filled by concrete: $E_b = 11.30$ GPa, $v_b = 0.25$ and $\rho_b = 2397.5$ kg/m^3.

The excitation is applied to a surface with length of 1.25 m in x-direction and of 2.5 m in y-direction (see Fig. 8). Such an excitation is applied to the model through a pressure p in z-direction, given by:

$$p = p_0 \sin(2\pi ft) \sin\left[\frac{\pi(t - t_a)}{t_d}\right] H(t - t_a) H(t_b - t)$$

(19)

for $p_0 = 1$ kN/m^2, $t_a = 0.0$ s, $t_b = 0.5$ s, and $f = 50$ Hz.

The damping ratio is taken to be equal to 1% for the ground and 6% for the barrier, whereas $f_p = 50$ Hz. By exploiting Eq.(6) and the above input data, the damping matrix **C** is computed.

3.2.2. Results

In Fig. 9(a), the vertical displacement reduction ratio r_{u_z} is plotted against the normalized coordinate x'/λ_{min}, being such a ratio defined as follows:

$$r_{u_z} = \frac{u_z^b(x')}{u_z(x')}$$

(20)

where u_z^b is the maximum value of u_z when the barrier is included into the ground, u_z is the maximum value of vertical displacement when the barrier is absent, and x' is the local abscissa shown in Fig. 8, with its origin at point with coordinates equal to (25.0;0.0;23.75) m. The dashed line corresponds to the case without damping (both in the ground and in the barrier), whereas the continuous line corresponds to the case with damping. The minimum wave length λ_{min} computed by using Eq. (17) is equal to 5.05 m. Fig. 9 shows that the model is quite sensitive to damping.

Note that the results reported in Refs. [55–57] are also plotted in Fig. 9(a). In such cases, the problem being examined is solved in frequency domain. A quite good agreement between the present results with damping and those taken from the literature can be noticed, especially for $1 \leqslant x'/\lambda_{min} \leqslant 3$.

The normalized vertical displacement, defined as the ratio between the maximum value of vertical displacement $u_z^b(x')$ and the maximum vertical displacement $u_{z,max}^b$ in the range $-5 \leqslant x' \leqslant 5$ m, when the barrier is included into the ground, is plotted in Fig. 9(b) against the normalized coordinate x'/λ_{min} (only the results for $0 \leqslant x' \leqslant 5$ m are plotted). The case without barriers is also examined. Both curves are obtained without damping.

Since the barrier is located at $x'/\lambda_{min} = 0$, it can be noted that the barrier is effective up to $x'/\lambda_{min} = 0.7$: as a matter of fact, over such a value, the vertical displacements can be amplified due to the barrier, as has also been remarked in a recent work by Carpinteri et al. [58].

In Fig. 10, both the elastic and the kinetic energy against time are plotted, with barrier (Fig. 10(a)) and without barrier (Fig. 10(b)). It can be noticed that the presence of the barrier produces a local increment of the oscillation in both elastic and kinetic energy.

4. Complex simulations by using the LDEM

The present Section is aimed to show the capability of LDEM to solve geotechnical problems which can hardly be solved with other numerical methods.

4.1. Simulation

4.1.1. Ground model through the LDEM

Ground and barrier properties are those used in Section 3.2.1. Furthermore, damage of the bars due to cracks nucleation and propagation of the ground is implemented in the model.

The excitation is applied (in two steps) to a surface with length of 1.25 m in x-direction and 2.5 m in y-direction (see Fig. 11).

Firstly, a vertical transient pulsed pressure characterized by a parabolic shape is applied. Its maximum value $p_{max} = 10$ MPa is attained at time instant 0.25 s, whereas the value $p = 7.5$ MPa is reached at time instants equal to both $t = 0.0125$ s and $t = 0.0375$ s. The total duration of such an excitation is 0.5 s. The effect of this excitation is to produce a smeared damage in the ground. Then, a second excitation is applied to the model by a pressure p acting in z-direction, described by the function given in Eq. (19), for
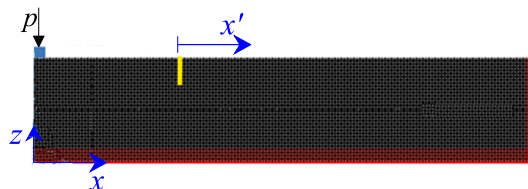

Fig. 8. LDEM model used in the basic simulation No. 2. The region of total absorption boundary condition is highlighted in red.
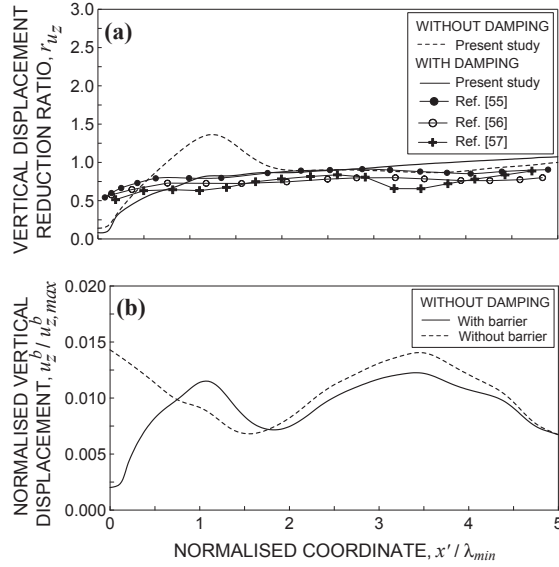
Fig. 9. Vertical displacement: (a) vertical displacement reduction ratio r_{u_z} vs x'/λ_{min} related to the present study, and data from the literature [55–57], (b) normalized vertical displacement $u_z^b/u_{z,max}^b$ vs x'/λ_{min}.
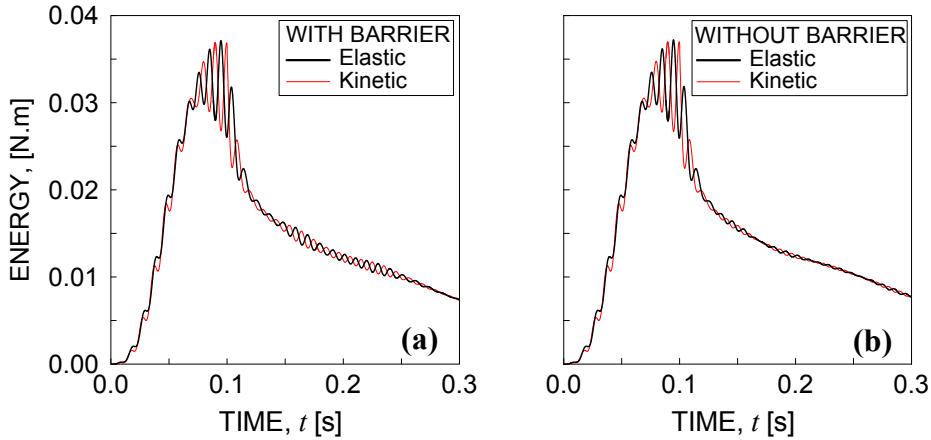

Fig. 10. Energy balance: elastic and kinetic energy (a) with barrier and (b) without barrier.
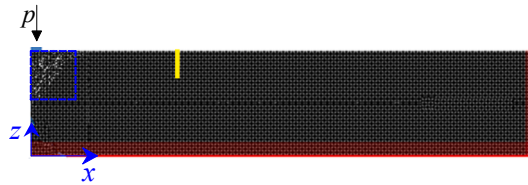

Fig. 11. LDEM model used in the complex simulation No. 1. The region of total absorption boundary condition is highlighted in red.

$p_0 = 0.1$ MPa, $t_a = 0.0$ s, $t_b = 0.5$ s, and $f = 50$ Hz.

In order to model the damage condition of the ground, the parameters discussed in Section 2 have to be fixed. The mean value of the specific fracture energy μ_{G_f} is equal to 50 N/m, and the strain at the peak load is equal $\varepsilon_p = 1.5 \, (10)^{-4}$. By employing Eq.(12), the value of the material characteristic length is computed: $d_{eq} = 6.92m$. The strain ε_r is equal to 0.003, being $A_n^*/A_n = 0.341$, $A_d^*/A_d = 0.349$, and $L_n = 0.50$ m.

In order to describe the statistical distribution of the specific fracture energy G_f (see Eq.(13)), the coefficient of variation CV_{G_f}, is taken equal to 0.8, whereas the correlation lengths L_{cx}, L_{cy} and L_{cz}, used to define the spatial correlation function of G_f, are equal to 0.50 m.
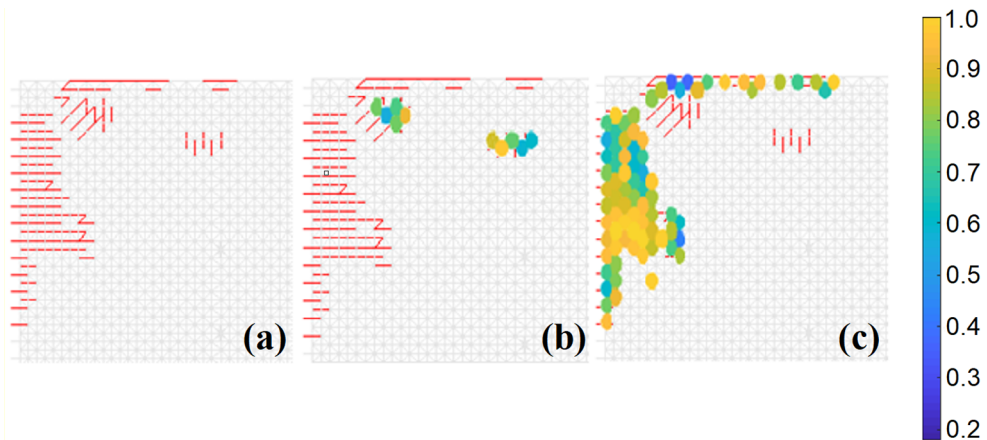
Fig. 12. Damage in the model region, highlighted by a dashed rectangle (with sizes 10 × 10 m) in Fig. 11, in terms of: (a) broken bar, (b) damage index for the broken bars oriented in z-direction, and (c) damage index for the broken bars oriented in x-direction.
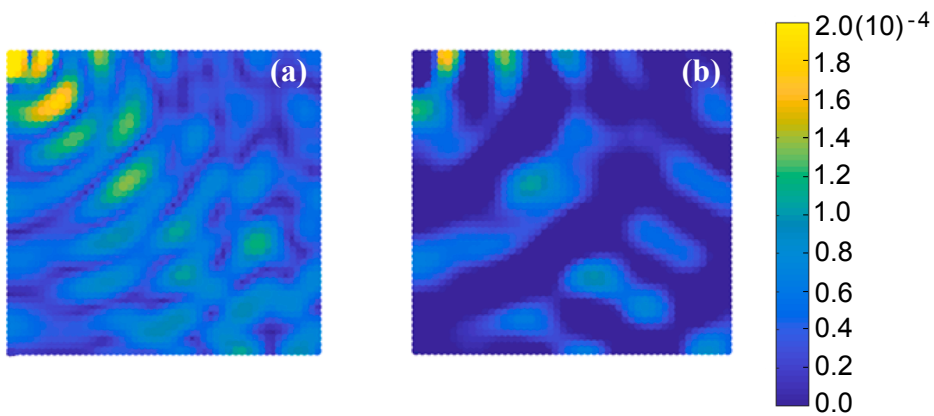

Fig. 13. Displacement magnitude (expressed in m) in the model region, highlighted by a dashed rectangle (with sizes 10 × 10 m) in Fig. 11: (a) only the second loading step is applied, (b) both loading steps are applied.
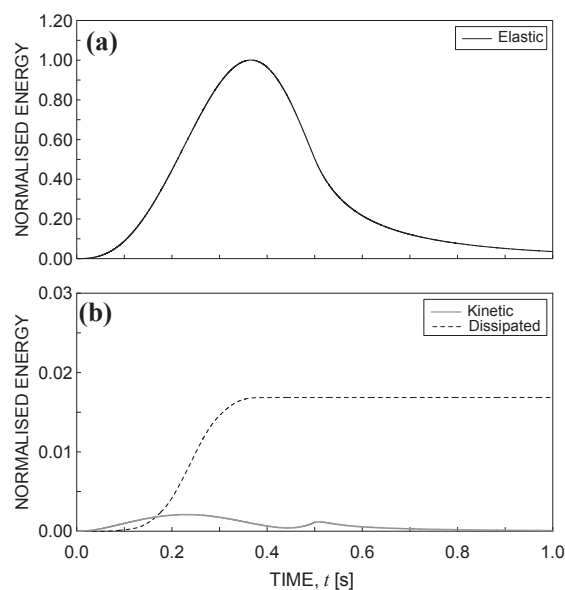

Fig. 14. Energy balance in terms of normalised energy: (a) elastic, and (b) kinetic and dissipated vs time, produced by the first loading step.
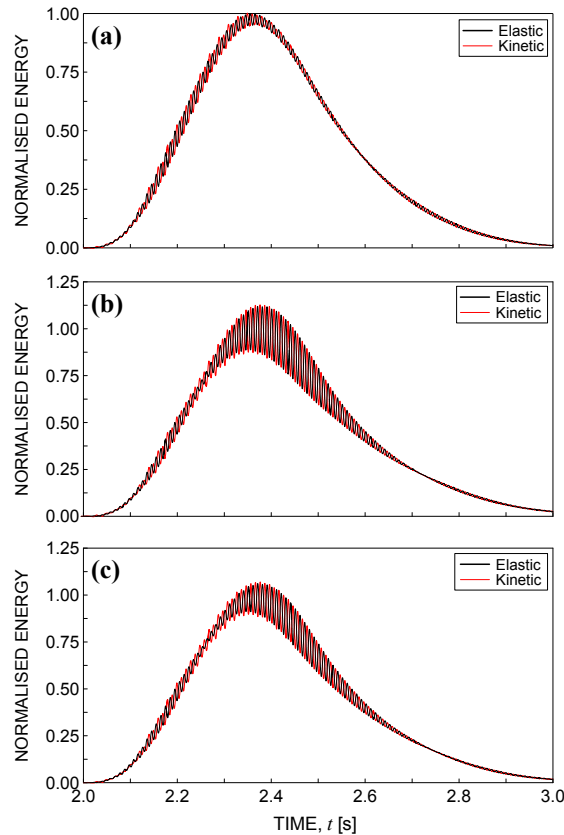
Fig. 15. Energy balance: (a) normalized energy (elastic and kinetic) against time without the barrier, (b) with barrier inside the ground, without damping, (c) with barrier inside the ground considering a damping for the barrier (damping ratio of 5%).

4.1.2. Results

Let us consider the bars related to the model region highlighted by a dashed rectangle in Fig. 11. In Fig. 12(a), the bars broken after the application of the first loading step are highlighted in red. The damage index, defined as the ratio between the elastic modulus of a broken bar over the elastic modulus of the ground, is plotted in Fig. 12(b), related to broken bars oriented in z-direction, whereas the damage index related to broken bars oriented in x-direction is plotted in Fig. 12(c). Such a damage condition is also that after the application of the second loading step, due to the low amplitude of such a step.

Fig. 13 shows the contour map of the displacement magnitude at time instant 2.25 s related to the above model region. More precisely, Fig. 13(a) refers to displacements when only the second loading step is applied to the model, whereas Fig. 13(b) refers to displacements when both loading steps are applied.

It can be observed in Fig. 13(b) that the ground damage region behaves as a filter of wave propagation due to the lack of both isotropy and homogeneity in such a region, whereas the wave pattern shape is concentric in Fig. 13(a).

The results in terms of energy balance are shown in Fig. 14. More precisely, the normalized energy (elastic, kinetic and dissipated), defined as the ratio between the energy value at a given time instant and the maximum value of such an energy registered during the simulation, is plotted against the time. Such normalized energies are those produced by the first loading step.

Let us consider a damping ratio equal to 5% for the barrier. The results in terms of energy balance are shown in Fig. 15. More precisely, the normalized energy (elastic, kinetic and dissipated) is plotted against the time, with and without the barrier. Such normalized energies are those produced by the second loading step.

In this case, the normalized energy is defined as the ratio between the energy value at a given time instant and the maximum value of such an energy registered during the simulation without barrier. It can be noticed that the barrier produces a considerable increase of both elastic and kinetic energy. The influence of the damping in terms of energy balance can be examined by comparing Fig. 15(b) with Fig. 15(c). As a matter of fact, it can be observed that the amplitude of the oscillation decreases in Fig. 15(c).

5. Conclusions

As is well-known, one of the main problems encountered in the numerical simulation of wave shielding by using vertical barriers is the ground modeling. To solve this problem, the LDEM has been herein employed to simulate both typical elastic-dynamic problems and a complex problem consisting in the simulation of the wave shielding produced by a vertical barrier into a damaged

ground where wave propagation occurs. More precisely, in the first part of the paper, the LDEM has been applied to two typical elastic-dynamic problems. Then, a more complex problem has been examined by considering damage of the ground. It has been shown that LDEM can be employed to accurately simulate problems of wave propagation in semi-infinite space. Further, the capability to include damage into ground has been shown, that makes the method an interesting tool for analysis of the actual problems.

Note that the input data used in the present simulations have been chosen in an arbitrary way. In the case of the simulation of experimental tests, a calibration of the numerical model in terms of the material properties is needed; further, the definition of the statistical properties of the whole random fields is needed and, consequently, more than one simulation has to be performed.

Acknowledgements

Appendix A. Supplementary material

Supplementary data to this article can be found online at https://doi.org/10.1016/j.engfailanal.2019.104360.

References

[1] E.D. Shumuye, A. Dinku, Investigation of the binding materials properties and assessment of durability issue in Fasil Ghibbi palace in Gondar, Eng. Fail. Anal. 93 (2018) 309–316.
[2] G. Alencar, A. de Jesus, J.G.S. da Silva, R. Calçada, Fatigue cracking of welded railway bridges: a review, Eng. Fail. Anal. 104 (2019) 154–176.
[3] S.E. Kattis, D. Polyzos, D.E. Beskos, Vibration isolation by a row of piles using a 3-d frequency domain BEM, Int. J. Numer. Meth. Eng. 46 (1999) 713–728.
[4] S.V. Kuznetsov, Reflection and scattering of seismic waves by seismic barriers, Int. J. Computat. Civil Struct. Eng. 7 (2011) 23–32.
[5] J. Huang, Z. Shi, Application of periodic theory to rows of piles for horizontal vibration attenuation, Int. J. Geomech. 13 (2013) 132–142.
[6] S.V. Kuznetsov, A new principle for protection from seismic waves, in: Proceedings of the International Conference on Performance-Based Design in Earthquake Geotechnical Engineering, Tokyo, Japan, 2009, pp. 463–468.
[7] S.V. Kuznetsov, Seismic waves and seismic barriers, Acoust. Phys. 57 (2011) 420–426.
[8] Y.B. Yang, H.H. Hung, A parametric study of wave barriers for reduction of train induced vibrations, Int. J. Numer. Meth. Eng. 40 (1997) 3729–3747.
[9] D.P. Connolly, G. Kouroussis, O. Laghrouche, C.L. Ho, M.C. Forde, Benchmarking railway vibrations – track, vehicle, ground and building effects, Constr. Build. Mater. 92 (2015) 64–81.
[10] P. Zoccali, G. Cantisani, G. Loprencipe, Ground-vibrations induced by trains: filled trenches mitigation capacity and length influence, Constr. Build. Mater. 74 (2015) 1–8.
[11] F. Yarmohammadi, R. Rafiee-Dehkharghani, C. Behnia, A.J. Aref, Topology optimization of jet-grouted overlapping columns for mitigation of train-induced ground vibrations, Constr. Build. Mater. 190 (2018) 838–850.
[12] E. Çelebi, S. Firat, G. Beyhan, I. Çankaya, I. Vural, O. Kirtel, Field experiments on wave propagation and vibration isolation by using wave barriers, Soil Dyn. Earthquake Eng. 29 (2009) 824–833.
[13] P.H. Tsai, T.S. Chang, Effects of open trench siding on vibration-screening effectiveness using the two-dimensional boundary element method, Soil Dyn. Earthquake Eng. 29 (2009) 865–873.
[14] A. Alzawi, M. Hesham El Naggar, Full scale experimental study on vibration scattering using open and in-filled (GeoFoam) wave barriers, Soil Dyn. Earthquake Eng. 31 (2011) 306–317.
[15] T. Xia, M. Sun, C. Chen, W. Chen, X. Ping, Analysis on multiple scattering by an arbitrary configuration of piles as barriers for vibration isolation, Soil Dyn. Earthquake Eng. 31 (2011) 535–545.
[16] S.D. Ekanayake, D.S. Liyanapathirana, C.J. Leo, Attenuation of ground vibrations using in-filled wave barriers, Soil Dyn. Earthquake Eng. 67 (2014) 290–300.
[17] A. Saikia, Numerical study on screening of surface waves using a pair of softer backfilled trenches, Soil Dyn. Earthquake Eng. 65 (2014) 206–213.
[18] Voyiadjis, G.Z. (Ed.). Handbook of damage mechanics: nano to macro scale for materials and structures. Springer-Verlag New York. 2015, doi: 10.1007/978-1-4614-5589-9.
[19] G.R. Liu, S. Jerry, S. Quek, A Non-reflecting boundary for analysing wave propagation using the finite element method, Finite Elem. Anal. Des. 39 (2003) 403–417.
[20] E. Haber, C. Cornou, D. Jongmansa, F.Youssef, D. Abdelmassihb, F. Lopez-Caballero, T. AL-Bittarb, Influence of 2D heterogeneous elastic soil properties on surface groundmotion spatial variability, Soil Dyn. Earthq. Eng. 2019;123:75–90.
[21] V.B. Puglia, L.E. Kosteski, J.D. Riera, I. Iturrioz, Random field generation of the material properties in the Lattice, Anal. Eng. Des. (2019), https://doi.org/10.1177/0309324719858849.
[22] R. Rodrigues, G. Birck, I. Iturrioz, Damage index proposals applied to quasi-brittle materials simulated using the lattice discrete element method, Int. J. Damage Mech. 25 (2016) 1017–873.
[23] S. Mastilovic, A. Rinaldi, Two-dimensional discrete damage models: discrete element methods, particle models, and fractal theories, in: handbook of damage mechanics, Editor Voyiadjis G Z. Springer New York, New York, NY, 2015, pp. 273–303.
[24] S.A. Silling, Reformulation of elasticity theory for discontinuities and long-range forces, J. Mech. Phys. Solids 48 (2000) 175–209.
[25] F. Bobaru, J.T. Foster, P.H. Geubelle, S.A. Silling, Handbook of peridynamic modeling, 1 ed., CRC Press, 2016.
[26] E. Madenci, E. Oterkus, Peridynamic theory and its applications. Vo. 17. Springer-Verlag, New York, 2014.
[27] P.A. Cundall, O.D.L. Strack, A discrete numerical model for granular assemblies, Géotechnique 29 (1979) 47–65.
[28] O'Sullivan C. Particulate Discrete Element Modelling: A Geomechanics Perspective. Applied Geothecnic vol 4. Spon Press, 2011.
[29] E. Schlangen, J.G.M. Van Mier, Crack propagation in sandstone: combined experimental and numerical approach, Rock Mech. Rock Eng. 28 (1995) 93–110.
[30] D. Krajcinovic, M. Vujosevic, Strain localization – short to long correlation length transition, Int. J. Solids Struct. 35 (1998) 4147–4166.
[31] Sagar R. Vidya, B.K. Raghu Prasad, Modelling heterogeneity of concrete using 2D lattice network for concrete fracture and comparison with AE study, Sadhana 34 (2009) 865–886.
[32] A. Rinaldi, Advances in statistical damage mechanics (SDM): new modeling strategies, In: Damage mechanics and micromechanics of localized fracture phenomena in inelastic solids, Springer Vienna, Vienna, 2001, pp. 105–224.
[33] M.R.A. van Vliet, Size effect in tensile fracture of concrete and rock, Ph.D. Thesis, Delft University of Technology, Delft, The Netherlands, 2000.
[34] J.D. Riera, Local effects in impact problems on concrete structures, in: Proceedings of the Conference on Structural Analysis and Design of Nuclear Power Plants, Porto Alegre, Brazil, 1984, 57–79.

[35] L. Koteski, I. Iturrioz, A.P. Cisilino, R. Barrios D'ambra, V. Pettarin, L. Fasce, P. Frontini, A lattice discrete element method to model the falling-weight impact test of PMMA specimens, Int. J. Impact Eng. 2016;87:120–131.

[36] J.D. Riera, I. Iturrioz, Discrete elements model for evaluating impact and impulsive response of reinforced concrete plates and shells subjected to impulsive loading, Nucl. Eng. Des. 179 (1998) 135–144.

[37] L.F.F. Miguel, I. Iturrioz, J.D. Riera, Size effects and mesh independence in dynamic fracture analysis of brittle materials, Comput. Model. Eng. Sci. 56 (2010) 1–16.

[38] J.D. Riera, L.F.F. Miguel, I. Iturrioz, Strength of brittle materials under high strain rates in DEM simulations, Comput. Model. Eng. Sci. 82 (2011) 113–136.

[39] L.E. Kosteski, I. Iturrioz, R. Barrios D'ambra, Crack propagation in elastic solids using the truss-like discrete element method, Int. J. Fract. 2012;174:139–161.

[40] L.E. Kosteski, J.D. Riera, I. Iturrioz, R.K. Singh, T. Kant, Analysis of reinforced concrete plates subjected to impact employing the truss-like Discrete Element Method, Fatigue Fract. Eng. Mater. Struct. 38 (2015) 276–289.

[41] I. Iturrioz, G. Lacidogna, A. Carpinteri, Acoustic emission detection in concrete specimens: experimental analysis and lattice model simulations, Int. J. Damage Mech. 8 (2013) 1–44.

[42] I. Iturrioz, G. Lacidogna, A. Carpinteri, Experimental analysis and truss-like discrete element model simulation of concrete specimens under uniaxial compression, Eng. Fract. Mech. 110 (2013) 81–98.

[43] G. Birck, I. Iturrioz, G. Lacidogna, A. Carpinteri, Damage process in heterogeneous materials analyzed by a lattice model simulation, Eng. Fail. Anal. 70 (2016) 157–176.

[44] A.B. Colpo, L.E. Kosteski, I. Iturrioz, The size effect in quasi-brittle materials: experimental and numerical analysis, Int. J. Damage Mech. 26 (2017) 395–416.

[45] L.A. Dalguer, K. Irikura, J.D. Riera, H.C. Chiu, The importance of the dynamic source effects on strong ground motion during the 1999 Chi-Chi, Taiwan, earthquake: brief interpretation of the damage distribution on buildings, Bull. Seismol. Soc. Am. 91 (2001) 1112–1127.

[46] J.D. Riera, I. Iturrioz, The Gutenberg-Richter and similar laws and their relation with numerical and experimental laboratory results, in: Proceedings of the 15th World Conf. on Earth. Eng., 2012.

[47] J.D. Riera, I. Iturrioz, Considerations on the diffuse seismicity assumption in stable continental regions (SCR), Int. J. Adv. Seismol. 1 (2014) 16–28.

[48] G. Birck, J.D. Riera, I. Iturrioz, Numerical DEM simulation of AE in plate fracture and analogy with the frequency of seismic events in SCRs, Eng. Fail. Anal. 93 (2018) 214–223.

[49] A.H. Nayfeh, M.S. Hefzy, Continuum modeling of three-dimensional truss-like space structures, AIAA J. 16 (1978) 779–787.

[50] A. Hillerborg, A Model for Fracture Analysis. Cod LUTVDG/TV BM-3005/1-8, 1978.

[51] B.M. Das, G.V. Ramana, Principles of Soil Dynamics, Cengage Learning, 2011.

[52] M. Aberg, P. Gudmundson, The usage of standard finite element codes for computation of dispersion relations in materials with periodic microstructure, J. Acoust. Soc. Am. 102 (1997) 2007–2013.

[53] R. Bruna, J.D. Riera, Towards the simultaneous generation of the three components of the seismic acceleration on rock surface, Nucl. Eng. Des. 110 (1988) 153–163.

[54] Groth E. Becker, I. Iturrioz, G.R.T. Clarke, The dispersion curve applied in guided wave propagation in prismatic rods, Latin Am. J. Solids Struct. 15 (2018) 1–27.

[55] T.M. Al-Hussaini, S. Ahmad, Design of wave barriers for reduction of horizontal ground vibration, J. Geotech. Geo environ. Eng. (ASCE) 117 (1991) 616–636.

[56] D. Beskos, G. Dasgupta, I. Vardoulakis, Vibration isolation using open or filled trenches, Part 1: 2-D homogeneous soil, Comput. Mech. 1 (1986) 43–63.

[57] Qiu B. Numerical study on vibration isolation by wave barrier and protection of existing tunnel under explosions. Civil Eng. INSA de Lyon, 2014, ffNNT: 2014ISAL0011f.

[58] A. Carpinteri, G. Fortese, C. Rochei, D. Scorza, A. Tasora, S. Vantadori, Dynamic shieldings for cultural heritage buildings under seismic action, Dyn. Earthq. Eng. 89 (2016) 269–276.